npj | computational materials

Article

Published in partnership with the Shanghai Institute of Ceramics of the Chinese Academy of Sciences

https://doi.org/10.1038/s41524-024-01263-0

Surface-dominated conductance scaling in Weyl semimetal NbAs

Sushant Kumar[1,2] ✉, Yi-Hsin Tu[3], Sheng Luo[4], Nicholas A. Lanzillo[5], Tay-Rong Chang[3], Gengchiau Liang[4], Ravishankar Sundararaman[1], Hsin Lin[6] & Ching-Tzu Chen[2] ✉

Protected surface states arising from non-trivial bandstructure topology in semimetals can potentially enable advanced device functionalities in compute, memory, interconnect, sensing, and communication. This necessitates a fundamental understanding of surface-state transport in nanoscale topological semimetals. Here, we investigate quantum transport in a prototypical topological semimetal NbAs to evaluate the potential of this class of materials for beyond-Cu interconnects in highly-scaled integrated circuits. Using density functional theory (DFT) coupled with non-equilibrium Green's function (NEGF) calculations, we show that the resistance-area *RA* product in NbAs films decreases with decreasing thickness at the nanometer scale, in contrast to a nearly constant *RA* product in ideal Cu films. This anomalous scaling originates from the disproportionately large number of surface conduction states which dominate the ballistic conductance by up to 70% in NbAs thin films. We also show that this favorable *RA* scaling persists even in the presence of surface defects, in contrast to *RA* sharply increasing with reducing thickness for films of conventional metals, such as Cu, in the presence of surface defects. These results underscore the potential of topological semimetals as future back-end-of-line (BEOL) interconnect metals.

The discovery of Weyl semimetals and topological semimetals in general[1–9] has prompted research into the discovery of new phenomena and their applications in various areas of condensed matter physics. These include usage as far-infrared and tetrahertz detectors[10], magnetoresistive memory devices[11,12], photovoltaic devices[13], and as interconnects in next-generation integrated circuits (ICs)[14–17]. A Weyl semimetal can be formed by breaking either time-reversal or inversion symmetry in a crystal with 3D Dirac cones, leading to pairs of band crossing points called Weyl nodes. The surface Brillouin Zone of Weyl semimetals have projections of such Weyl node pairs connected through series of topologically-protected Fermi-arc surface states[3]. Substantial recent research efforts have targeted first-principles prediction of new topological semimetals, material syntheses, and confirmation of nontrivial band structures and Fermi-arc surface states using angle-resolved photoemission spectroscopy (ARPES)[5–9]. These materials have been shown to exhibit unconventional transport, optical and magnetic phenomena[18–21], including chiral anomalies[22], a nonlinear Hall effect[23–25], a quantized circular photogalvanic effect[26–28] and giant second-harmonic generation[10,29].

Like topological insulators, the surface states of topological semimetals have received considerable attention, which if topologically protected, could potentially lead to high surface conduction. Previous theoretical work has argued that the Fermi-arc states in a toy-model Weyl semimetal contribute the same order of magnitude as the bulk states to total conduction[30] and could be highly disorder tolerant when the Fermi arcs are nearly straight[31]. However, other studies have shown that the transport due to Fermi arcs is dissipative due to a strong hybridization of surface and bulk states, which leads to scattering between surface and bulk states[32,33]. Since these studies relied primarily on highly-simplified Hamiltonians and analytical models, a comprehensive study of transport fully accounting for the electronic structure at dimensions relevant to future device applications is now necessary.

In this work, we pursue a fundamental understanding of electron transport properties of Weyl semimetals at nanoscale and evaluate their potential as high conductivity future interconnect metals. In modern-day ICs, the devices patterned on a silicon substrate are linked to form a circuit using Cu nanowires called interconnects. The resistivity of Cu increases

[1]Department of Materials Science & Engineering, Rensselaer Polytechnic Institute, 110 8th St, Troy, NY 12180, USA. [2]IBM Thomas J. Watson Research Center, 1101 Kitchawan Road, Yorktown Heights, NY 10598, USA. [3]Department of Physics, Cheng Kung University, Tainan City, Taipei. [4]Department of Electrical and Computer Engineering, College of Design and Engineering, National University of Singapore, Singapore, Singapore. [5]IBM Research, 257 Fuller Road, Albany, NY 12203, USA. [6]Institute of Physics, Academia Sinica, Taipei, Taipei. ✉e-mail: Sushant.Kumar@ibm.com; cchen3@us.ibm.com

dramatically with decreasing size due to enhanced scattering of electrons from surfaces, defects, and grain boundaries[34–37]. Such increase in the resistivity can increase the signal delay and energy consumption by ~40×, a major bottleneck in the semiconductor industry[16,38]. The search to replace Cu has expanded from elemental metals to intermetallics[39–42], metallic carbides and nitrides such as MAX phases[43,44], directional conductors[45], and topological materials[14,15,17,46,47].

In a recent breakthrough, Zhang et al.[48] showed experimentally that the electrical resistivity of nanobelts of [001] oriented NbAs, a Weyl semimetal, becomes an order of magnitude lower than the bulk single-crystal resistivity. In some nanobelt samples, the resistivity can even be lower than the bulk resistivity of Cu. Such an anomalous reduction was attributed to transport via the disorder-tolerant Fermi-arc surface states in NbAs. Furthermore, using first-principles calculations, Chen et al.[14] predicted that thin films of a prototypical chiral topological semimetal CoSi can exhibit conduction dominated by Fermi-arc surface states, leading to an resistance-area (*RA*) product that decreases with decreasing thickness, in stark contrast to Cu and other conventional metal films.

Despite the promising trend of decreasing *RA* product with dimensions, CoSi is still at a disadvantage compared to Cu because of the low density of states at the Fermi level and a significantly higher bulk resistivity. Hence, we need semimetals with larger numbers of topologically-protected surface states[14,17]. The aforementioned Weyl semimetal NbAs is one such candidate with 12 pairs of Weyl nodes. In this work, we use first-principles quantum transport calculations to predict the *RA* product scaling of (001) NbAs thin films with and without surface defects. We find that the *RA* product decreases with decreasing film thickness for both pristine and defect-laden films, as previously shown for CoSi[14]. However, NbAs does not exhibit the protection of surface transport protected against line-defects that was shown for CoSi due to the chiral nature of its surface states. Our calculations illustrate that the observed *RA* scaling in NbAs is due to the large number of surface states that account for at least 50% of conduction for films thinner than ~7 nm. The contribution of the Nb-terminated surfaces in (001) NbAs films is roughly 3 times that of the As-terminated surfaces. Lastly, we show that surface-mediated conduction and favorable *RA* scaling with thickness survives in the presence of minor surface disorder.

Results

Bandstructure and Fermi surface

Figure 1b shows the first-principles-computed bandstructures of 16 atomic-layer (AL) (~21.43 Å) and 40 AL (~56.71 Å) (001) slabs of NbAs. The colors represent the contribution of spatial regions to each electronic state: bulk in gray, Nb-terminated surface in red and As-terminated surface in blue. Increasing the thickness of the slabs (16 AL → 40 AL) increases the number of bulk bands but the surface bands remain largely unchanged. Note that the (001) surface of NbAs reduces the C_4 rotational symmetry of the bulk to C_2[1,49]. As a result, both the Nb-terminated (red) and As-terminated (blue) surface bands differ between the Γ-X and Γ-Y high-symmetry **k**-point paths. The bulk (gray) bands, which dominate the Y-Γ-X path, however, are mostly symmetric about Γ. At the Fermi level, the Nb-terminated surface bands are hole-like along X-Γ-Y and electron-like along M-Y-Γ-X. These results agree with previous DFT bandstructure calculations for NbAs films[49].

Next, we analyze the Fermi surfaces of (001) NbAs slabs to get insight into its electronic bandstructure. Since electronic states at the Fermi level dominate conduction, we aim to find the chemical potential at which the DFT-predicted isoenergy surfaces agree the best with ARPES data[4] to use for subsequent non-equilibrium Green's function (NEGF) calculations. Figure 2 shows the isoenergy surfaces for a 56 AL slab computed using the Wannierized electronic states (**k**-point grid: 512 × 512) at different energy levels ε near the neutral Fermi level ε_F, with $\varepsilon - \varepsilon_F \in \{-120, -80, -40, 0\}$ meV. As described in the Methods section, these isoenergy surfaces have been resolved by contributions of the bulk (gray), Nb-terminated (red) and As-terminated (blue) surfaces.

Comparing the top and bottom rows, we find that a disproportionate number of states belong to the Nb-terminated surface. Sun et al.[49]

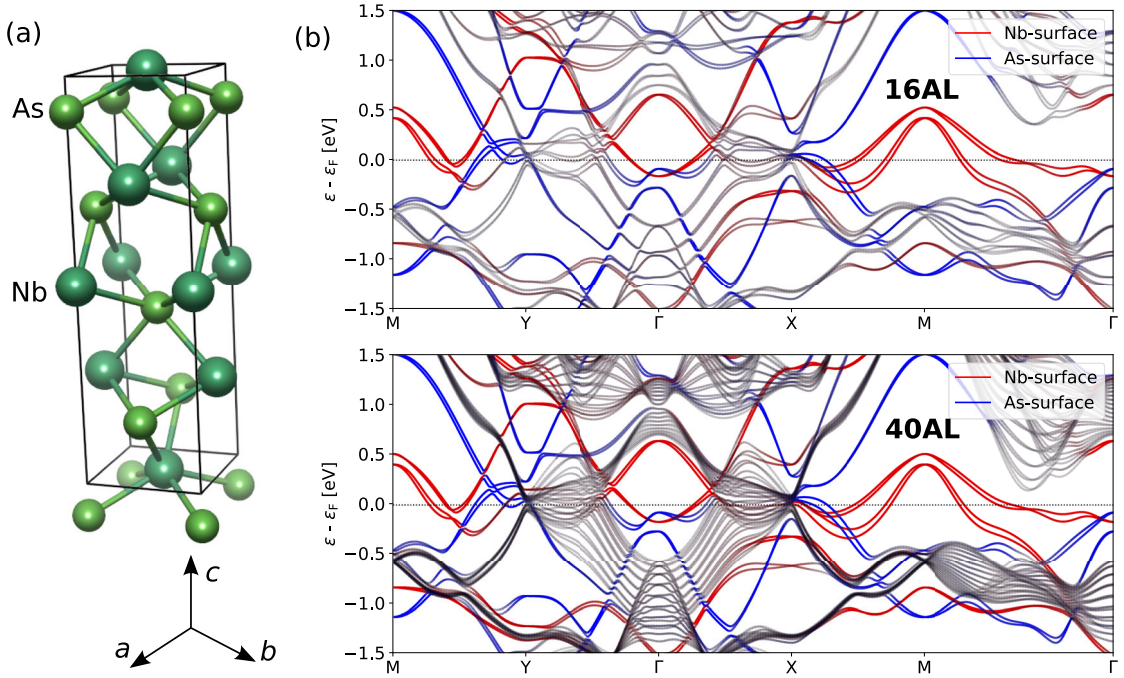

Fig. 1 | Crystal structure of bulk NbAs and bandstructures of thin films of NbAs. **a** The tetragonal unit cell of NbAs comprises 8 atomic layers such that each Nb and As atom has a coordination number of 6. The crystal has time-reversal symmetry but lacks a space-inversion symmetry. When a bulk NbAs crystal is cleaved along (001) surface, it produces a Nb-terminated surface (top) and an As-terminated surface (bottom). **b** DFT bandstructures for 16AL and 40AL (001) films of NbAs with colors representing the contribution of the bulk (gray), Nb-terminated (red) and As-terminated (blue) surfaces to the electronic states. Increasing the thickness of slabs, increases the number of bulk bands at the Fermi level though the surface bands remain largely unchanged.

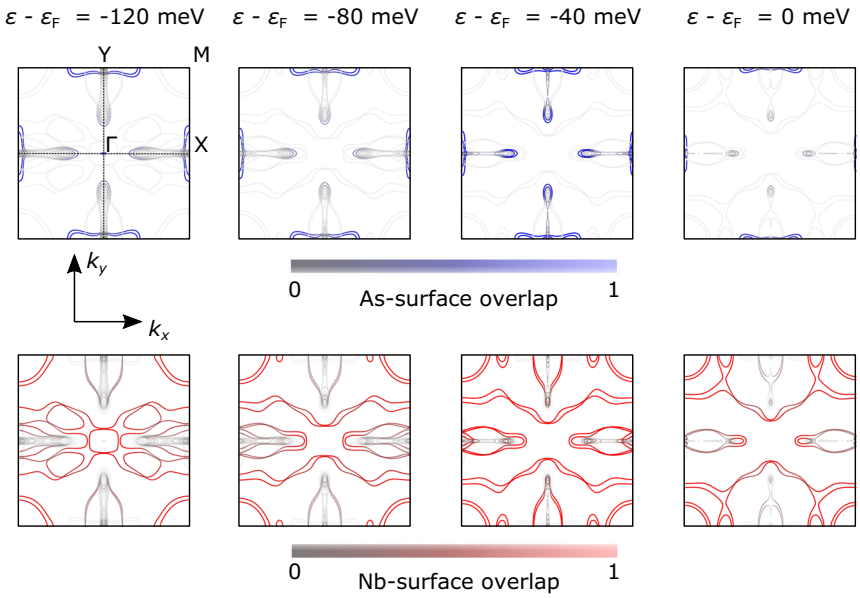

Fig. 2 | Fermi surfaces of NbAs slabs. Isoenergy surfaces for a relaxed 56AL (001) slab of NbAs (thickness ~80.24 Å) at energies ε = 120, 80, 40 and 0 meV below the neutral Fermi level ε_F. The colors represent the contribution of the bulk (gray), Nb-terminated surface (red) and As-terminated surface (blue) to the electronic states. The Nb-terminated surface contributes many more states that extend throughout the Brillouin zone, compared to the fewer As-terminated surface states that are localized in the **k**-space. The Fermi arc states agree with ARPES measurements best for $\varepsilon - \varepsilon_F = -80$ meV.

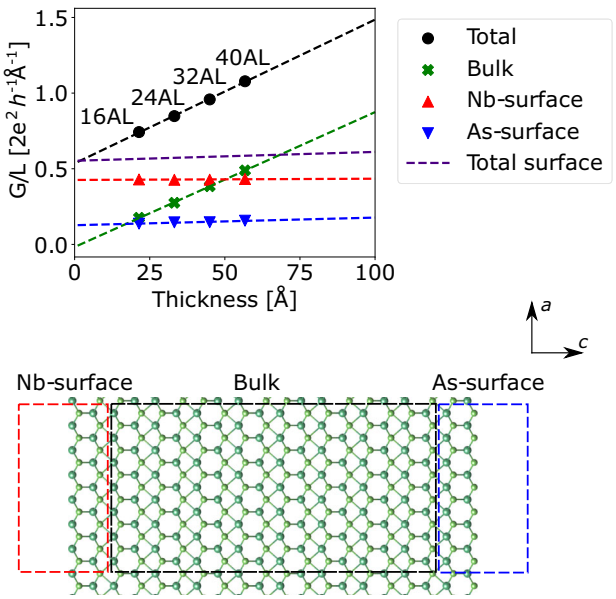

Fig. 3 | Contribution of the bulk and surface to the net ballistic conductance. Ballistic conductance as a function of thickness for pristine (001) NbAs films. The total conductance increases linearly due to the linear increase in bulk conductance, while the conductance contribution due to surface states remains constant. The dashed lines are linear fits to the computed data points for 16, 24, 32 and 40 AL slabs. Surface conduction dominates over bulk conduction for slabs thinner than 6.8 nm, reaching 76% of the total conduction for 2-nm-thick slabs.

noted that strong hybridization between the surface and bulk states, and between trivial Fermi surfaces and arcs, makes it difficult to isolate the topological Fermi-arc states. However, careful analysis of spin textures[49] and ARPES measurements[4] has indicated that the outer arc of the spoon-shaped features along Γ-X and Γ-Y are the Fermi arcs. These arcs are not clearly visible at the DFT-predicted Fermi level ε_F, but become clearer with decreasing ε and achieve good agreement with the ARPES measurements of the As-terminated surface at $\varepsilon - \varepsilon_F = -80$ meV. Hence, we shift the Fermi level down by 80 meV from the original DFT-computed value for all transport predictions reported below.

Ballistic conductance scaling

We first compute the ballistic conductance of pristine films of NbAs as a function of thickness using

$$G = \frac{e^2}{2}\int_{BZ}\sum_b g_s \frac{d\mathbf{k}}{(2\pi)^3} f_0'(\varepsilon_{\mathbf{k}b})|v^x_{\mathbf{k}b}| \quad (1)$$

where $\varepsilon_{\mathbf{k}b}$ and $\mathbf{v}_{\mathbf{k}b}$ are the electronic energies and velocities of band b and wavevector $\mathbf{k}$ in the Brillouin zone (BZ) and g_s is the spin degeneracy factor (g_s = 1 for the $\varepsilon_{\mathbf{k}b}$ vs. $\mathbf{k}$ relations with spin-orbit coupling). The derivative of the Fermi-Dirac occupations $f_0'(\varepsilon_{\mathbf{k}b})$ limits the contributions of electronic states to within a few k_BT around the Fermi level ε_F (Refer SI for a detailed derivation of Equation (1)). We evaluate the above expression in JDFTx[50] for room temperature (k_BT = 0.026 eV) using a Monte Carlo sampling of 250,000 **k**-points in the BZ. We also decompose the total conductance G into contributions from bulk, Nb-terminated and As-terminated surfaces by weighing each electronic state in the integrand of Eq. (1) with a slab weight function described in the Methods sections. The bounding box or slab used to define the spatial region for the surface states has been shown in Fig. 3. Note that we use this approach to predict ballistic conductance in pristine films, which would have no scattering.

We see that the total ballistic conductance per unit length (G/L) increases linearly with thickness (Fig. 3). The decomposition of the total conductance into bulk and surface contributions shows that the Nb- and As-terminated surface-state contributions remain constant with thickness. This thickness independence of the surface states (and hence, the conductance) is supported by the electronic bandstructures of the slabs (Fig. 1b) and the Fermi-surface plots resolved by the contribution of each atomic layer (Supplementary Figs. 12 and 13). As noted in the previous section, the surface states (red and blue bands) remain remarkably the same as we increase the thickness from 16AL to 40AL. We only see an increase in the number of bulk bands (gray). Supplementary Figs. 12 and 13 show that the penetration depths of the surface states are roughly 0.6 nm (~6AL) for both the Nb- and As-terminated surfaces. Hence, the surface states would remain untangled as long as the thickness of the slabs is more than 12AL (i.e., slabs with 2 or more unit cells along the z-direction). Consequently, for slabs of such thickness there would be almost no hybridization of the states emanating from the opposite surfaces.

The bulk conductance contribution decreases linearly with decrease in film thickness and extrapolates to nearly zero for zero thickness. Hence, the

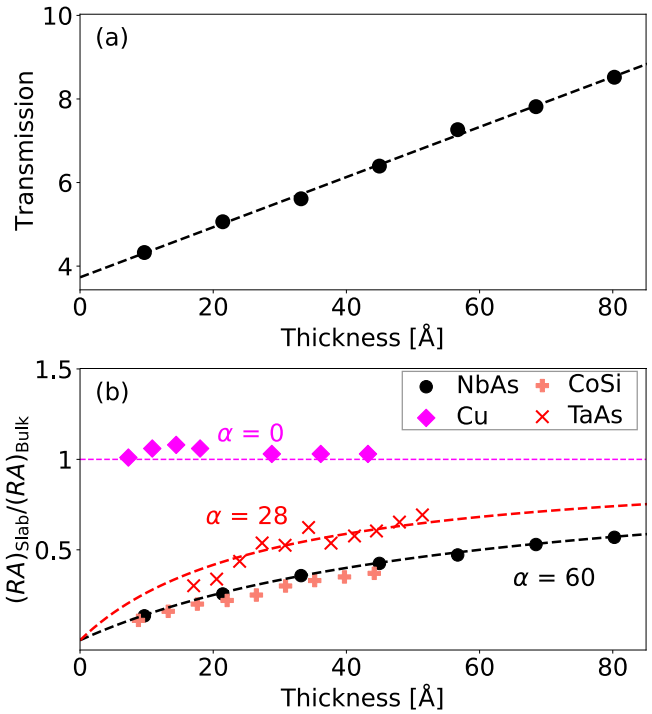

Fig. 4 | Comparison of the ballistic conductance of pristine thin films of different materials. a Transmission as a function of thickness for pristine (001) slabs of NbAs. The non-zero intercept corresponds to surface conduction. **b** Normalized resistance-area *RA* product for transport along [100] direction of NbAs (001) slabs, compared against [001] transport direction of (100)-terminated surfaces of CoSi & Cu and [001] transport direction for (100)-terminated surface of TaAs taken from ref. 14. The dashed line is the fit of Equation (4) to the computed conductance data for NbAs. Topological semimetals NbAs and CoSi show a promising trend of decreasing *RA* product with decreasing thickness due to the significant contribution of surface states to total conductance for thin films of both materials.

total conductance G can be expressed as

$$G = g_{\text{bulk}}t + G^{\text{Nb}}_{\text{surf}} + G^{\text{As}}_{\text{surf}} \quad (2)$$

where t is the thickness of the film, g_{bulk} is the slope of the linear fit to bulk conductance and $G^{\text{Nb}}_{\text{surf}}$ and $G^{\text{As}}_{\text{surf}}$ are the conductance due to Nb- and As-terminated surfaces respectively. For a 16 AL (~2.1 nm) slab, the surface states and bulk account for 76.3% and 23.7% of the total ballistic conductance respectively. Such large surface state contributions to conductance have been observed for other topological semimetals as well, e.g. ~90% surface-state contribution in 2.7-nm-thick CoSi[47]. As we increase the thickness to 40 AL (~5.7 nm), the bulk conductance contribution for NbAs increases to 45.4% while the surface contribution reduces to 54.6%. Extrapolation of the linear fits to bulk and total surface conductance ($G^{\text{Nb}}_{\text{surf}} + G^{\text{As}}_{\text{surf}}$) reveals that the crossover point where surface and bulk conductance become equal is at around 6.8 nm which corresponds to a relaxed 48 AL slab. We also find that due to the larger number of states at the Fermi level, the ballistic conductance of NbAs (001) films is larger than that of CoSi (See Supplementary Fig. 8). Specifically, for a 2.5-nm-thick slab, the conductance for NbAs is around 57% higher than that of CoSi.

Importantly, the Nb-terminated surface contributes almost 3 times as much as the As-terminated surface to ballistic conductance, i.e., $G^{\text{Nb}}_{\text{surf}} \approx 3G^{\text{As}}_{\text{surf}}$. This is in line with the Nb-terminated surface states vastly outnumbering the As-terminated surface states in the surface-resolved Fermi surfaces shown in Fig. 2.

Note that shifting the boundary of the bounding box/slab further into the slab (Fig. 3) would count more electronic states as surface states, including a part of the bulk conductance into the surface. While the definition of these boundaries is arbitrary, we have chosen it to the maximum value for which $G^{\text{Nb/As}}_{\text{surf}}$ remains thickness independent in order to capture as much of the surface state contribution as possible, without including the bulk.

Resistance-area product scaling

We next analyze the resistance-area (*RA*) product scaling for films of NbAs with and without defects (pristine) and compare the results with those of Cu (a conventional metal) and CoSi (a chiral multifermion semimetal) (Fig. 4a).

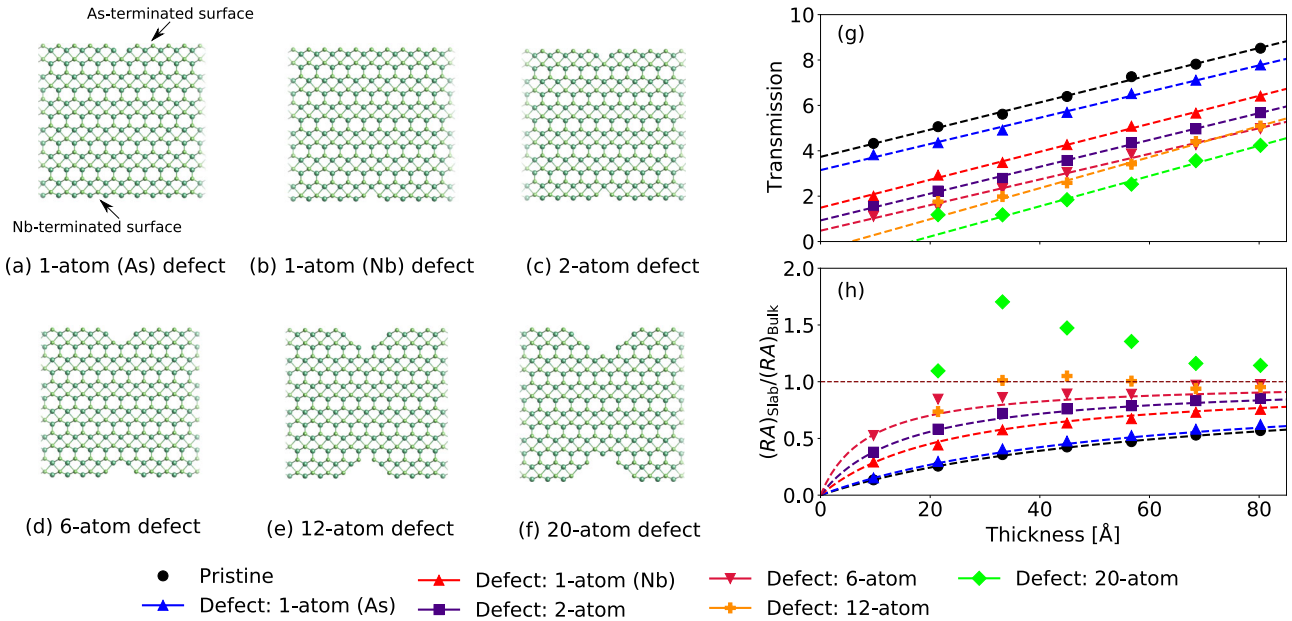

Fig. 5 | Effect of different defect configurations on the electron transport in NbAs slabs. a–f Illustration of the different surface line-defect configurations studied in our NEGF calculations. **g** Transmission and **h** normalized resistance-area *RA* product for [100] transport in NbAs(001) with defects. Line defects reduce the net transmission, but the intercept remains nonzero and the corresponding *RA* remains below the bulk value, indicating that surface conduction persists. Only when the notch is made deep enough, such as for the 20-atom defect, the *RA* product begins to increase with decreasing thickness due to a significant reduction in the transmission.

The resistance R of these films have been calculated using the transmission T at the Fermi level ε_F using

$$R = \frac{1}{G_0 T(\varepsilon = \varepsilon_F)} \tag{3}$$

Here, G_0 is the quantum of conductance e^2/h. The transmission is computed using the NEGF method[51], where we employ Wannier tight-binding Hamiltonians constructed using DFT as described in the Methods section.

Previous first-principles NEGF calculations have shown that the RA product of slabs $(RA)_{slab}$ for pristine Cu is mostly independent of slab thickness[14,47,52], because bulk states dominate conduction. A similar trend has also been observed for MoP, a topological metal, where most of the electronic states at the Fermi level are bulk states[46]. Hence, for such materials, conductance $G(=1/R)$ decreases linearly with decreasing thickness or cross-sectional area A, making the RA product constant. Consequently, independent of film thickness, the normalized RA product $(RA)_{slab}/(RA)_{bulk} \approx 1$.

In contrast, NEGF calculations of pristine films of NbAs show that $(RA)_{slab}$ decreases with decreasing film thickness and is always less than $(RA)_{bulk}$, similar to previous reports for CoSi films[14,47]. This can be explained by extending Equation (2) to calculate $(RA)_{slab}/(RA)_{bulk}$

$$(RA)_{slab}/(RA)_{bulk} \approx \frac{1}{1 + \alpha/t} \tag{4}$$

where $\alpha = (G^{Nb}_{surf} + G^{As}_{surf})/g_{bulk}$ (See Supplementary Note 3). For a material where the conduction is dominated by bulk states and the contribution of surface states is negligible, the value of α would be very small ($\alpha \to 0$). Conversely, materials like topological insulators, which exhibit zero bulk conductance and finite surface conductance would have $\alpha \to \infty$. Hence, the parameter α essentially quantifies where we are on the spectrum between a topological insulator and a conventional metal.

Equation (4) predicts that $(RA)_{slab} < (RA)_{bulk}$ in pristine slabs of any finite thickness t, as long as there is some surface contribution, $\alpha > 0$. When surface conductance is negligible, $G_{surf} \to 0$ leading to $\alpha \to 0$, we find normalized $RA \to 1$ for all thicknesses, exactly as observed for conventional metals such as Cu. Agreement between the computed $(RA)_{slab}/(RA)_{bulk}$ and Equation (4) (Fig. 4b) establishes the validity of the simple model of additive surface and bulk conductance for Weyl semimetals.

We now investigate the effect of notches or surface line-defects on the ballistic conductance of NbAs films. We study six different types of defects as shown in Fig. 5a–f. The calculated transmission and the resultant normalized RA product are shown in Fig. 5g and h, respectively. As expected, the transmission for pristine films increases linearly with thickness, which corresponds to the increasing number of bulk conducting channels/bands at the Fermi level. We perform a linear fit ($y = mx + b$) for the thickness-dependent transmission data for all defect types. (The parameters slope m, intercept b and R^2 have been provided in Supplementary Table 1. We also use these parameters to compute the RA product curves that would be expected if the transmission against thickness was a perfectly straight line as shown in Fig. 5h)). Removing an As atom from the As-terminated (top) surface leads to a relatively small drop in the transmission for all the slabs, such that the intercept of the linear fit drops only slightly, $\Delta b \sim -0.6$. However, removing a Nb atom from the Nb-terminated (bottom) surface causes an almost 4 times larger reduction ($\Delta b \sim -2.2$) in the transmission. For the third case (Fig. 5c), where we remove an atom each from the top and bottom surface, the transmission reduces by ~2.8, which is equal to the sum of the above two reductions. As we increase the depth of the 'notch' on the surfaces (Fig. 5d–f), the net transmission continues to diminish. We note that the total transmission extrapolated to zero thickness remains finite in films with single-atom, 2-atom, and 6-atom line-defects, indicative of the survival of surface-state conduction in films with sufficiently small disorder. With the deep 12-atom and 20-atom defects, the transmission reduction levels off for the thinnest film and leads to the downturn in the RA product with scaling as shown in Fig. 5h. This is similar to the resistivity scaling trend reported previously for CoSi films with high surface defect densities[47].

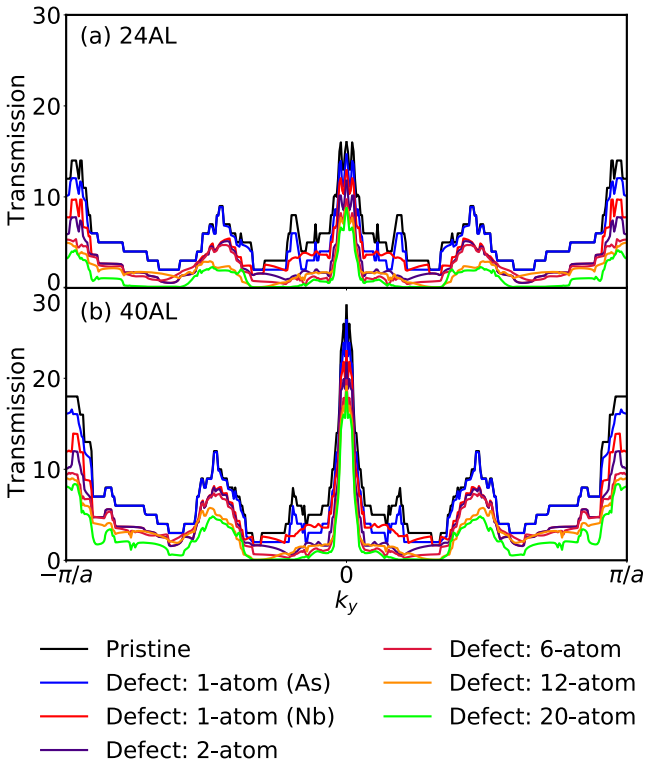

Fig. 6 | Momentum k-resolved transmission of films of NbAs with surface line-defects. Increasing the thickness of the NbAs (001) slabs (results shown for 24AL and 40AL) increases the transmission (higher peaks) owing to the larger number of bulk states. Except for the case of 1-atom (As) defect configuration, line defects reduce the transmission at every **k**-point indicating the absence of protection. For the 1-atom defect, where an atom is removed from the As-terminated surface, transmission is not affected in regions of the Brillouin zone which do not have the localized As-surface states.

To further understand the above observations, we analyze the **k**-resolved transmission for two representative cases of 24AL and 40AL slabs. Figure 6 shows the transmission plotted against direction k_y which is the in-plane direction normal to the transport direction k_x. Since the transmission for pristine films essentially represents the number of states at the Fermi level, the values are integers for any k_y. As the thickness increases, we see an increase in the peak heights around $k_y \sim 0$, $k_y \sim \pm 0.45\pi/a$, and $k_y \sim \pm \pi/a$ corresponding to the increasing number of bulk states around those points in the Brillouin Zone (See Supplementary Fig. 7). In general, defects reduce the transmission, though by varying degree as noted in Fig. 5g. The 1-atom defect on the As-terminated surface negligibly changes the transmission for $k_y \sim [-0.9\pi/a, -0.47\pi/a]$ and $k_y \sim [0.47\pi/a, 0.9\pi/a]$, because there are no surface states on the As-terminated surface in that region (Supplementary Fig. 7). Consequently, the localization of As-terminated surface states in the **k**-space leads to the small overall change in transmission. Most of the surface states at the Fermi level that contribute to conduction exist on the Nb-terminated surface, as shown previously in Fig. 3. Correspondingly, a defect on the Nb-terminated surface considerably reduces the transmission throughout k_y, since the Nb-terminated states extend throughout the projected 2D Brillouin Zone. The 2-atom defect, removing one Nb and one As atom on each surface, reduces the transmission by roughly the sum of the previous two cases. We find the transmission reduces further for every point along k_y for 6-atom, 12-atom and 20-atom defects.

Using the net transmission calculated above, we plot the normalized RA product in Fig. 5h for the various defect configurations. Since the transmission T continues to exhibit a roughly linear dependence on

thickness t for the cases with defects, we could employ a model similar to Equation (4) to fit the computed data. Specifically, we write $G = G_0T(\varepsilon_F) = G_0(mt + b)$. Comparing to Equation (4), we note that $\alpha = b/m$. We find that the normalized RA product for the first four defect types exhibit a trend similar to the pristine case, i.e. $(RA)_{slab}/(RA)_{bulk}$ decreases with decreasing thickness. Since the net transmission doesn't change significantly for the 1-atom defect on the As-terminated surface, its normalized RA curve (blue) is very close to the case with no defects (black) in Fig. 5h. Increasing the size of the defects makes the (RA) vs. t curves flatter, as the normalized RA product begins to become thickness independent and approaches 1 when the surface state conduction gradually diminishes, manifested in the intercept of transmission b approaching zero. Thus, in the limit of sufficiently strong surface disorder, the Weyl semimetal behaves more like a conventional metal in this respect. For example, the 12-atom and 20-atom defect configurations begin to kill the transmission of the bulk states besides significantly suppressing surface conduction, which makes the RA product of the slab greater than that of the ideal bulk.

As a further proof that the transport in NbAs films is indeed dominated by surface states, we perform calculations for the cases where line-defects are introduced in the bulk (center) of the slabs (see Supplementary Fig. 9a–c). Supplementary Fig. 9d shows that the bulk line-defects do not have any significant impact on the normalized resistance-area product of the films. While a 2-atom surface defect reduces the transmission by around 44% for a 4-nm slab (32AL), a 2-atom bulk defect decreases the corresponding transmission by only ~5%. This can be seen more clearly in the momentum-resolved transmission where the bulk line-defects have negligible effect on the transmission across the Brillouin zone (Supplementary Fig. 10). These results reinforce our observation that the conduction is overwhelmingly dominated by surface states. Only surface defects significantly reduce the transmission and consequently, affect the resistance-area scaling.

It is important to note that for very thin films, the 12-atom and 20-atom defect configurations are large enough to significantly perturb the electronic states in the region near the defect. In our current approach, however, the tight-binding models are based on the ground state of the pristine films, and the couplings linked to the removed atom are deleted to mimic the defect. Therefore, the calculated transmissions at 16 AL and below for these two defect configurations are likely to be less reliable than the remaining cases. Although more accurate results can be obtained using self-consistent DFT and NEGF in QuantumATK[53], it can be computationally expensive and potentially prohibitive for large-thickness structures with spin-orbit coupling, as studied here. Nevertheless, the qualitative trend discussed above that the transmission levels off in the ultra-thin film limit is also demonstrated by the fully self-consistent DFT with NEGF calculations using QuantumATK[53] (Supplementary Fig. 1).

Though the transmission has been predicted for single line-defects in this work, the results can be extended to more realistic systems with multiple defects (The details of this approach can be found in the Supplementary Note 5). Supplementary Fig. 2 shows that the resistivity of NbAs films in the diffusive limit decreases with thickness in the presence of weak surface disorder. This scaling trend of decreasing resistivity is similar to the resistance-area scaling observed for the films with single line-defects. However, as the surface transport is not well protected for NbAs, the resistivity first increases before decreasing as we increase the depth of the line-defects.

Finally, we compare the conductance scaling of NbAs films with that of CoSi. Both materials show decreasing RA with reduced thickness in pristine films, owing to the dominance of surface conduction over bulk conduction at the nanometer scale. However, CoSi is a chiral semimetal with forward- and backward-moving surface carriers from the Fermi-arc states of the same transverse momentum spatially separated on opposite surfaces of a CoSi thin film[14]. Consequently, line defects which preserve the transverse momentum cannot backscatter these states into each other and the transmission of the CoSi Fermi arc states is robust against such defects[14]. In contrast, the forward- and backward-moving surface carriers with the same transverse momentum coexist on both surfaces of NbAs, and thus can

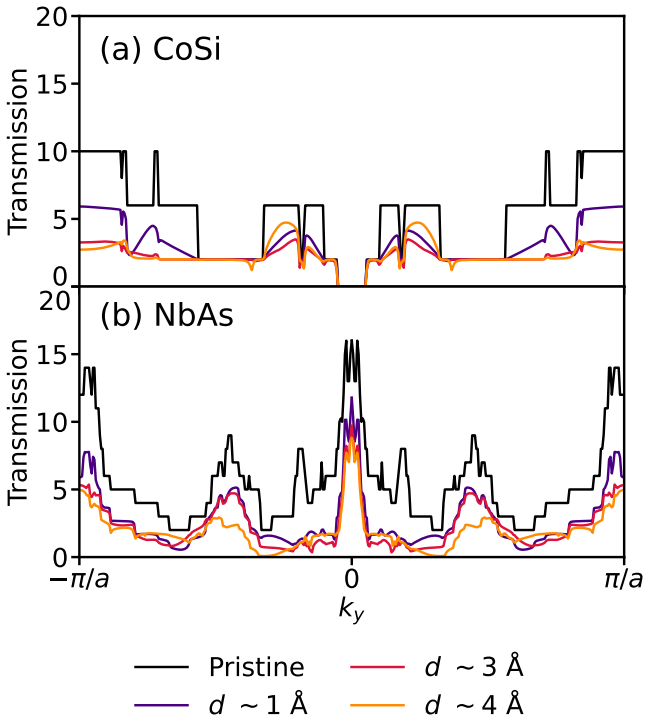

Fig. 7 | Comparison of the electron transport mechanism in CoSi and NbAs films. Momentum k-resolved transmission for (001)-oriented slabs of **a** CoSi (3.3-nm thick) and **b** NbAs (3.4-nm thick) in the presence of different surface line-defects. For the case of CoSi, there is one state per spin whose forward- and backward-moving surface states do not lie on the same surface due to chirality, and hence, their transmission never goes below 2 (accounting for spin degeneracy) as they cannot backscatter. However, the transmission is reduced throughout the Brillouin zone for NbAs since the forward- and backward-moving states lie on the same surface and so are not protected from backscattering.

intermix (see Supplementary Fig. 11). Therefore, transmission of the NbAs Fermi-arc states is much more susceptible to defect scattering. As shown in Fig. 7, a line-defect can reduce the transmission for all **k**-points in the Brillouin zone, contrary to that in the CoSi films. This explains the substantial reduction of total transmission in NbAs films with single-atom defects (see Fig. 5). Supplementary Fig. 14 shows the NEGF-predicted transmissions and resultant RA products for the two materials. To make a fair comparison, we introduce surface line-defects of comparable depths. Unlike in the case of CoSi where a decreasing RA trend persists for deeper defects, in NbAs, we begin to observe a near-reversal (i.e., RA product starts to increase with decreasing thickness) for a 4-Å-deep notch. This is consistent with our observation above that the transport is more robust to surface defects in CoSi (a chiral topological semimetal) than in NbAs. We also note that though the RA product begins to flatten out earlier for NbAs, the absolute value of the RA product is still lower (i.e., higher conductance) than that of CoSi, because NbAs has a higher number of conducting surface states at the Fermi level than CoSi.

Experimentally, the 2-3 orders of magnitude increase in resistivity observed in ~600 nm diameter NbAs nanowires[4] when compared to the micron-size wide nanobelts demonstrates the sensitivity of the NbAs surface states to defect scattering at the boundaries. Therefore, for materials with optimal disorder-tolerant surface-state conductivity, future work should explore *chiral* topological semimetals. In addition, while both NbAs and CoSi beat Cu in terms of the normalized-RA product (i.e., RA_{Slab}/RA_{Bulk}) for thinner films, in absolute terms the RA product of Cu is significantly lower than that of either of the two topological semimetals in pristine films because Cu has many more conducting states at the Fermi level to start with. Hence, even with the loss of transmission in the presence of defects, Cu may still outperform CoSi and NbAs. Therefore, it's imperative to search for

topological semimetals that are both chiral in their structure and also have large numbers of Fermi arcs to maximize the conducting chiral surface states.

Discussion

In summary, we performed first-principles NEGF calculations to understand the mechanism of electron transport in thin films of a representative Weyl semimetal, NbAs. The resistance-area *RA* product in pristine NbAs films decreases with thickness at the nanometer scale, in contrast to a nearly constant *RA* product in ideal Cu films. This anomalous scaling is the manifestation of the numerous surface states in the bandstructure of NbAs. The surface states account for over 70% of the conductance for 2.1-nm-thick (relaxed 16 AL) films and ~50% for 6.8-nm-thick (relaxed 48 AL) films; furthermore, contribution from the Nb-terminated surface states is almost 3 times that of the As-terminated-surface states. The decreasing *RA* with reducing dimensions persists even with surface defects, as long as the degree of disorder is moderate. This contrasts the ever increasing *RA* with reducing dimensions in conventional metals like Cu when disorder is present, and highlights the promise of Weyl semimetals, and topological semimetals in general, for integrated circuits. Finally, analyses of electron transmission in **k**-space show that electron transport in NbAs is not immune to defect scattering because forward- and backward-moving states coexist on the same surface, in contrast to the protected chiral surface transport in CoSi thin films. The comparison between the two material systems calls for the search for *chiral* topological semimetals with large numbers of Fermi arcs for low-resistance nanoscale interconnects.

Methods

First-principles calculations

We use open-source plane-wave DFT software JDFTx[50] for the generation of self-consistent relaxed crystal structures, electron bandstructures and Wannier tight-binding models. We use the fully-relativistic optimized norm-conserving Vanderbilt pseudopotentials (ONCVPSP)[54] as distributed by the open-source PSEUDODOJO library[55] to include spin-orbit coupling self-consistently. These DFT calculations are performed using the Perdew-Burke-Ernzerhof (PBE) generalized gradient approximation (GGA) to the exchange-correlation functional[56] at a plane-wave cutoff of 40 Hartrees and a charge density cutoff of 200 Hartrees.

For the first-principles study of NbAs slabs, we construct films of (001) orientation to allow direct comparison of our computed Fermi surfaces with the available ARPES results, which have been experimentally measured for the cleaved (001) surfaces[1,49]. These slabs have tetragonal unit cells, and are constructed with a vacuum spacing of 12 Å thickness along the *c*− direction, employing Coulomb truncation to eliminate long-range interactions between periodic images along this direction[57–59]. Cleaving the surface along (001) direction leads to two asymmetric surfaces with Nb and As terminations respectively (Fig. 1a), which produces an overall dipole moment in the unit cell. Supplementary Fig. 3 shows that the Coulomb truncation scheme accounts for this dipole correctly and produces zero electric field in the vacuum region away from both surfaces.

With the computational setup described above, we first perform an optimization of the ionic positions and lattice parameters of the body-centered tetragonal unit cell of bulk NbAs (space group $I4_1md$). The initial crystal structure was obtained from the Materials Project database[60]. The relaxation yields lattice constants of $a = b = 3.46$ Å and $c = 11.80$ Å which are within ~1% of the XRD measured values of $a = 3.45$ Å and $c = 11.68$ Å (Fig. 1a)[1,61]. Starting from a single-unit-cell thick slab, we then construct films with seven different thicknesses in steps of 1 unit cell. Hence, the thickness of our films vary from 1 unit cell or 8 atomic layers (AL) to 7 unit cells or 56 atomic layers (AL). Previous first-principles calculations for NbAs have found no noticeable change in the band structure and Fermi surfaces for slabs larger than 7 unit cells in thickness[49]. The DFT calculations for the bulk and slabs are performed using **k**-point meshes of $8 \times 8 \times 2$ and $8 \times 8 \times 1$, respectively, and Fermi smearing with width 0.01 Hartrees. Keeping the in-plane lattice constants of the slabs fixed ($a = b$), we optimize the ionic positions using self-consistent DFT for subsequent calculations of electronic bands, Fermi surface and electron transport properties.

Creating tight-binding models

We then construct a tight-binding model using a maximally-localized Wannier function basis set[62] in JDFTx. Supplementary Fig. 3 shows the contribution of *s*−, *p*− and *d*− orbitals of Nb and As atoms to each band for a 16AL slab. The electron bands in the energy range ± 6.5 eV around the Fermi level are mostly composed of the *d*− and *p*− orbitals of Nb and As atoms respectively. Hence, we choose a basis set of 10 *d*− orbitals per Nb atom and 6 *p*− orbitals per As atom in the unit cell as the initial guesses. We construct maximally-localized Wannier functions for our ab initio tight-binding model that reproduces the DFT bands in the energy window of $\varepsilon_F - \sim 7.3$ eV to $\varepsilon_F + \sim 2.9$ eV above ε_F, as shown in Supplementary Fig. 5.

Calculating surface and bulk contributions

To pinpoint the contributions of surface and bulk contributions to the band structure, Fermi surfaces and conductance in the Wannier basis, we compute weights of each Wannier-interpolated electronic state from the surface regions. Specifically, we define functions $w^X(z)$ for X = Nb and As, which are 1 within the dashed rectangles shown in the bottom panel of Fig. 3, and 0 outside it. We then compute the matrix elements $w^X_{\mathbf{k}ab} \equiv \int_\Omega d\mathbf{r} \psi^*_{\mathbf{k}a}(\mathbf{r}) \bar{w}^X(z) \psi_{\mathbf{k}b}(\mathbf{r})$, where $\bar{w}^X(z)$ is $w^X(z)$ smoothed by convolution with a Gaussian of width 1 bohr. Finally, we interpolate $w^X_{\mathbf{k}ab}$ using the Wannier representation in exactly the same way as the Hamiltonian and momentum matrix elements described in detail elsewhere[63,64].

Non-equilibrium Green's Function calculations

Using the tight-binding models created above, we employ Non-equilibrium Green's Function (NEGF) method to compute the electron transport properties of the films[51]. For the slab of NbAs, we consider transport along the [100] direction and calculate the total transmission as

$$T(E) = \int dk_y T(k_y, E) \tag{5}$$

where $T(k_y, E) = Tr(\Gamma_L G^R \Gamma_R G^A)$ is the k_y-resolved transmission and k_y is the in-plane direction. Here, $G^R(k_y, E) = [E + i\eta - H_{C,k_y} - \Sigma(k_y, E)]$ is the retarded Green's function, H_{C,k_y} is the tight-binding Hamiltonian of channel, and $\Sigma(k_y, E) = \Sigma_L(k_y, E) + \Sigma_R(k_y, E)$ is the contact self-energy of the left (L) and right (R) contact. $G^A(k_y, E)$ is the advanced Green's function, and $\Gamma_\alpha = i(\Sigma_\alpha - \Sigma_\alpha^\dagger)$ is the broadening of the contact-α($\alpha = L, R$). The contact self-energies are numerically solved using the Sancho-Rubio's method[65]. For the bulk of NbAs, similarly, the transmission can be written as

$$T(E) = \int dk_y dk_z T(k_y, k_z, E) \tag{6}$$

where the k_z is the out-of-plane direction for the bulk. We use k-point sampling of $400\, k_y$ and $800\, k_y \times 800\, k_z$ for slab and bulk transport calculation, respectively. The Hamiltonian of the channel H_C is constructed from the slab tight-binding model. In order to consider surface defect configurations in the channel, we remove the orbitals of atoms entirely from the Hamiltonian of channel H_C. Supplementary Fig. 6 shows the schematic view of structure for NEGF calculation for 24AL slab of NbAs with 12-atom defect configuration.

We, however, note that the method described here would be too expensive for predicting how impurity scattering in the form of point defects could affect the scaling trends. One could use the method recently proposed by Lien et al.[47] for this purpose. Additionally, our study does not include the effect of electron-phonon scattering which is beyond the scope of this work and is an important direction for future studies.

Data availability

All relevant data are available from the authors upon request.

Code availability

First-principles methodologies available through open-source software, JDFTx, and post-processing scripts available from authors upon request.

Received: 21 December 2022; Accepted: 10 April 2024;
Published online: 02 May 2024

References

1. Xu, S.-Y. et al. Discovery of a weyl fermion semimetal and topological fermi arcs. *Science* **349**, 613–617 (2015).
2. Yang, L. et al. Weyl semimetal phase in the non-centrosymmetric compound TaAs. *Nat. Phys.* **11**, 728–732 (2015).
3. Lv, B. et al. Experimental discovery of weyl semimetal TaAs. *Phys. Rev. X* **5**, 031013 (2015).
4. Xu, S.-Y. et al. Discovery of a weyl fermion state with fermi arcs in niobium arsenide. *Nat. Phys.* **11**, 748–754 (2015).
5. Armitage, N., Mele, E. & Vishwanath, A. Weyl and dirac semimetals in three-dimensional solids. *Rev. Mod. Phys.* **90**, 015001 (2018).
6. Lv, B., Qian, T. & Ding, H. Experimental perspective on three-dimensional topological semimetals. *Rev. Mod. Phys.* **93**, 025002 (2021).
7. Hasan, M. Z. et al. Weyl, dirac and high-fold chiral fermions in topological quantum matter. *Nat. Rev. Mater.* **6**, 784–803 (2021).
8. Yan, B. & Felser, C. Topological materials: Weyl semimetals. *Annu. Rev. Condens. Matter Phys.* **8**, 337–354 (2017).
9. Bansil, A., Lin, H. & Das, T. Colloquium: Topological band theory. *Rev. Mod. Phys.* **88**, 021004 (2016).
10. Wu, L. et al. Giant anisotropic nonlinear optical response in transition metal monopnictide weyl semimetals. *Nat. Phys.* **13**, 350–355 (2017).
11. Han, J. et al. Current-induced switching of a ferromagnetic weyl semimetal co2mnga. *Appl. Phys. Lett.* **119**, 212409 (2021).
12. De Sousa, D., Ascencio, C., Haney, P. M., Wang, J.-P. & Low, T. Gigantic tunneling magnetoresistance in magnetic weyl semimetal tunnel junctions. *Phys. Rev. B* **104**, L041401 (2021).
13. Osterhoudt, G. B. et al. Colossal mid-infrared bulk photovoltaic effect in a type-i weyl semimetal. *Nat. Mater.* **18**, 471–475 (2019).
14. Chen, C.-T. et al. Topological semimetals for scaled back-end-of-line interconnect beyond cu. In *2020 IEEE International Electron Devices Meeting (IEDM)*, 32–4 (IEEE, 2020).
15. Han, H. J., Liu, P. & Cha, J. J. 1d topological systems for next-generation electronics. *Matter* **4**, 2596–2598 (2021).
16. Gall, D. et al. Materials for interconnects. *MRS Bull.* **46**, 1–8 (2021).
17. Lanzillo, N. A., Bajpai, U., Garate, I. & Chen, C.-T. Size-dependent grain-boundary scattering in topological semimetals. *Phys. Rev. Appl.* **18**, 034053 (2022).
18. Nagaosa, N., Morimoto, T. & Tokura, Y. Transport, magnetic and optical properties of weyl materials. *Nat. Rev. Mater.* **5**, 621–636 (2020).
19. Hu, J., Xu, S.-Y., Ni, N. & Mao, Z. Transport of topological semimetals. *Annu. Rev. Mater. Res.* **49**, 207–252 (2019).
20. Wang, S., Lin, B.-C., Wang, A.-Q., Yu, D.-P. & Liao, Z.-M. Quantum transport in dirac and weyl semimetals: a review. *Adv. Phys.: X* **2**, 518–544 (2017).
21. Gorbar, E., Miransky, V., Shovkovy, I. & Sukhachov, P. Anomalous transport properties of dirac and weyl semimetals. *Low. Temp. Phys.* **44**, 487–505 (2018).
22. Ong, N. & Liang, S. Experimental signatures of the chiral anomaly in dirac–weyl semimetals. *Nat. Rev. Phys.* **3**, 394–404 (2021).
23. Sodemann, I. & Fu, L. Quantum nonlinear hall effect induced by berry curvature dipole in time-reversal invariant materials. *Phys. Rev. Lett.* **115**, 216806 (2015).
24. Ma, Q. et al. Observation of the nonlinear hall effect under time-reversal-symmetric conditions. *Nature* **565**, 337–342 (2019).
25. Kang, K., Li, T., Sohn, E., Shan, J. & Mak, K. F. Nonlinear anomalous hall effect in few-layer wte2. *Nat. Mater.* **18**, 324–328 (2019).
26. de Juan, F., Grushin, A. G., Morimoto, T. & Moore, J. E. Quantized circular photogalvanic effect in weyl semimetals. *Nat. Commun.* **8**, 1–7 (2017).
27. Rees, D. et al. Helicity-dependent photocurrents in the chiral weyl semimetal rhsi. *Sci. Adv.* **6**, eaba0509 (2020).
28. Ni, Z. et al. Giant topological longitudinal circular photo-galvanic effect in the chiral multifold semimetal cosi. *Nat. Commun.* **12**, 1–8 (2021).
29. Patankar, S. et al. Resonance-enhanced optical nonlinearity in the weyl semimetal taas. *Phys. Rev. B* **98**, 165113 (2018).
30. Breitkreiz, M. & Brouwer, P. W. Large contribution of fermi arcs to the conductivity of topological metals. *Phys. Rev. Lett.* **123**, 066804 (2019).
31. Resta, G., Pi, S.-T., Wan, X. & Savrasov, S. Y. High surface conductivity of fermi-arc electrons in weyl semimetals. *Phys. Rev. B* **97**, 085142 (2018).
32. Gorbar, E., Miransky, V., Shovkovy, I. & Sukhachov, P. Origin of dissipative fermi arc transport in weyl semimetals. *Phys. Rev. B* **93**, 235127 (2016).
33. Wilson, J. H., Pixley, J., Huse, D. A., Refael, G. & Sarma, S. D. Do the surface fermi arcs in weyl semimetals survive disorder? *Phys. Rev. B* **97**, 235108 (2018).
34. Fuchs, K. The conductivity of thin metallic films according to the electron theory of metals. *Math. Proc. Camb. Philos. Soc.* **34**, 100 (1938).
35. Sondheimer, E. The mean free path of electrons in metals. *Adv. Phys.* **50**, 499–537 (2001).
36. Mayadas, A., Shatzkes, M. & Janak, J. Electrical resistivity model for polycrystalline films: the case of specular reflection at external surfaces. *Appl. Phys. Lett.* **14**, 345–347 (1969).
37. Mayadas, A. & Shatzkes, M. Electrical-resistivity model for polycrystalline films: the case of arbitrary reflection at external surfaces. *Phys. Rev. B* **1**, 1382 (1970).
38. Gall, D. The search for the most conductive metal for narrow interconnect lines. *J. Appl. Phys.* **127**, 050901 (2020).
39. Soulié, J.-P., Tőkei, Z., Swerts, J. & Adelmann, C. Aluminide intermetallics for advanced interconnect metallization: thin film studies. In *2021 IEEE International Interconnect Technology Conference (IITC)*, 1–3 (IEEE, 2021).
40. Chen, L., Ando, D., Sutou, Y., Gall, D. & Koike, J. Nial as a potential material for liner-and barrier-free interconnect in ultrasmall technology node. *Appl. Phys. Lett.* **113**, 183503 (2018).
41. Chen, L. et al. Interdiffusion reliability and resistivity scaling of intermetallic compounds as advanced interconnect materials. *J. Appl. Phys.* **129**, 035301 (2021).
42. Zhang, M. & Gall, D. Resistivity scaling in epitaxial cual 2 (001) layers. *IEEE Trans. Electron Devices* **69**, 5110–5115 (2022).
43. Sankaran, K., Moors, K., Tőkei, Z., Adelmann, C. & Pourtois, G. Ab initio screening of metallic max ceramics for advanced interconnect applications. *Phys. Rev. Mater.* **5**, 056002 (2021).
44. Zhang, M., Kumar, S., Sundararaman, R. & Gall, D. Resistivity scaling in epitaxial max-phase ti4sic3 (0001) layers. *J. Appl. Phys.* **130**, 034302 (2021).
45. Kumar, S., Multunas, C., Defay, B., Gall, D. & Sundararaman, R. Ultralow electron-surface scattering in nanoscale metals leveraging fermi-surface anisotropy. *Phys. Rev. Mater.* **6**, 085002 (2022).
46. Han, H. J. et al. Topological metal mop nanowire for interconnect. *Adv. Mater.* **35**, 2208965 (2023).
47. Lien, S.-W. et al. Unconventional resistivity scaling in topological semimetal cosi. *npj Quantum Mater.* **8**, 3 (2023).

48. Zhang, C. et al. Ultrahigh conductivity in weyl semimetal nbas nanobelts. *Nat. Mater.* **18**, 482–488 (2019).
49. Sun, Y., Wu, S.-C. & Yan, B. Topological surface states and fermi arcs of the noncentrosymmetric weyl semimetals taas, tap, nbas, and nbp. *Phys. Rev. B* **92**, 115428 (2015).
50. Sundararaman, R. et al. Jdftx: Software for joint density-functional theory. *SoftwareX* **6**, 278 – 284 (2017).
51. Datta, S.*Quantum transport: atom to transistor* (Cambridge university press, 2005).
52. Timoshevskii, V., Ke, Y., Guo, H. & Gall, D. The influence of surface roughness on electrical conductance of thin cu films: An ab initio study. *J. Appl. Phys.* **103**, 113705 (2008).
53. Smidstrup, S. et al. Quantumatk: An integrated platform of electronic and atomic-scale modelling tools. *J. Phys. Condens. Matter* **32**, 015901 (2020).
54. Hamann, D. Optimized norm-conserving vanderbilt pseudopotentials. *Phys. Rev. B* **88**, 085117 (2013).
55. van Setten, M. J. et al. The pseudodojo: Training and grading a 85 element optimized norm-conserving pseudopotential table. *Comput. Phys. Commun.* **226**, 39–54 (2018).
56. Perdew, J. P., Burke, K. & Ernzerhof, M. Generalized gradient approximation made simple. *Phys. Rev. Lett.* **77**, 3865 (1996).
57. Sundararaman, R. & Arias, T. Regularization of the coulomb singularity in exact exchange by wigner-seitz truncated interactions: Towards chemical accuracy in nontrivial systems. *Phys. Rev. B* **87**, 165122 (2013).
58. Ismail-Beigi, S. Truncation of periodic image interactions for confined systems. *Phys. Rev. B* **73**, 233103 (2006).
59. Rozzi, C. A., Varsano, D., Marini, A., Gross, E. K. & Rubio, A. Exact coulomb cutoff technique for supercell calculations. *Phys. Rev. B* **73**, 205119 (2006).
60. Jain, A. et al. The Materials Project: A materials genome approach to accelerating materials innovation. *APL Mater.* **1**, 011002 (2013).
61. Boller, H. & Parthé, E. The transposition structure of nbas and of similar monophosphides and arsenides of niobium and tantalum. *Acta Crystallogr.* **16**, 1095–1101 (1963).
62. Marzari, N., Mostofi, A. A., Yates, J. R., Souza, I. & Vanderbilt, D. Maximally localized wannier functions: Theory and applications. *Rev. Mod. Phys.* **84**, 1419–1475 (2012).
63. Habib, A., Florio, F. & Sundararaman, R. Hot carrier dynamics in plasmonic transition metal nitrides. *J. Opt.* **20**, 064001 (2018).
64. Kumar, S., Multunas, C. & Sundararaman, R. Fermi surface anisotropy in plasmonic metals increases the potential for efficient hot carrier extraction. *Phys. Rev. Mater.* **6**, 125201 (2022).
65. Sancho, M. L., Sancho, J. L. & Rubio, J. Quick iterative scheme for the calculation of transfer matrices: application to mo (100). *J. Phys. F: Met. Phys.* **14**, 1205 (1984).

Acknowledgements

S.K and R.S. acknowledge funding from Semiconductor Research Corporation under Task no. 2966.002. Calculations were carried out at the Center for Computational Innovations at Rensselaer Polytechnic Institute. The work at the National University of Singapore was supported by MOE-2017-T2-2-114, MOE-2019-T2-2-215, and FRC-A-8000194-01-00. T.-R.C. was supported by 2030 Cross-Generation Young Scholars Program from the Science and Technology Council (MOST111-2628-M-006-003-MY3), Cheng Kung University, and the Center for Theoretical Sciences. We gratefully acknowledge the helpful discussions with Daniel Gall (RPI), Utkarsh Bajpai (IBM) and Vijay Narayanan (IBM).

Author contributions

S.K. and Y.-H.T. performed the first-principles calculations and analyzed the data. S.K. and C.-T.C. wrote the manuscript with input from all the authors. C.-T.C. conceived and supervised the project.

Competing interests

The authors declare no competing interests.

Additional information

Supplementary information The online version contains supplementary material available at https://doi.org/10.1038/s41524-024-01263-0.

Correspondence and requests for materials should be addressed to Sushant Kumar or Ching-Tzu Chen.